NANO LETTERS

Letter

pubs.acs.org/NanoLett

Versatile Fabrication of Self-Aligned Nanoscale Hall Devices Using Nanowire Masks

Jianshi Tang,*[,†] Guoqiang Yu,[†] Chiu-Yen Wang,[‡] Li-Te Chang,[†] Wanjun Jiang,[†] Congli He,[†] and Kang L. Wang*[,†]

[†]Device Research Laboratory, Department of Electrical Engineering, University of California, Los Angeles, California 90095, United States

[‡]Department of Materials Science and Engineering, National Taiwan University of Science and Technology, Taipei City, Taiwan 10607, Republic of China

Supporting Information

ABSTRACT: In this work, we present an ingenious method to fabricate self-aligned nanoscale Hall devices using chemically synthesized nanowires as both etching and deposition masks. This versatile method can be extensively used to make nanoribbons out of arbitrary thin films without the need for extremely high alignment accuracy to define the metal contacts. The fabricated nanoribbon width scales with the mask nanowire width (diameter), and it can be easily reduced down to tens of nanometers. The self-aligned metal contacts from the sidewall extend to the top surface of the nanoribbon, and the overlap can be controlled by tuning the deposition recipe. To demonstrate the feasibility, we have fabricated Ta/CoFeB/MgO nanoribbons sputtered on a SiO_2/Si substrate with different metal contacts, using synthesized SnO_2 nanowires as masks. Anomalous Hall effect measurements have been carried out on the fabricated nanoscale Hall device in order to study the current-induced magnetization switching in the nanoscale heavy metal/ferromagnet heterostructure, which has shown distinct switching behaviors from micron-scale devices. The developed method provides a useful fabrication platform to probe the charge and spin transport in the nanoscale regime.

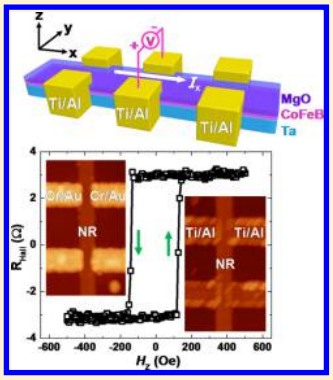

KEYWORDS: *Nanowire, nanoribbon, self-aligned contacts, Hall effect, current-induced magnetization switching*

As an important group of quasi-one-dimensional (1-D) nanomaterials, nanowires and nanoribbons (also known as nanobelts) have attracted enormous research interest for their unique physical properties. For example, they naturally provided a 1-D channel for carrier (including both charge and spin), photon, and phonon transport with significant quantum confinements in the other two dimensions. Their broad applications as building blocks for nanoelectronics have been explored, including field-effect transistors (FETs) and logic units,[1−5] chemical, biological, and mechanical sensors,[6−9] optoelectronic devices,[10−12] and emerging nanotechnologies.[13−16] For the material preparation, the fabrication of nanoribbons and nanowires has been extensively studied using both bottom-up approach from self-assembled chemical synthesis and top-down approach from templated etching and patterning.[17−21] In general, while the chemical synthesis approach typically offers the advantages of low cost and convenient processing, the highly organized templated etching approach could provide better uniformity, controllability, and compatibility with mainstream silicon technology.

In bridging these two approaches, self-assembled nanowires have also been used as versatile etching masks to transfer their 1-D morphology onto arbitrary underlying substrate, such as silicon and graphene,[5,22−29] producing nanoribbons with controllable widths no larger than the nanowire diameters. There have also been attempts to use nanowires as deposition mask to make self-aligned contacts for short-channel graphene transistors.[30−32] This so-called nanowire lithography provides a very convenient method to fabricate nanoribbons on arbitrary substrates without complex high-resolution optical lithography or electron beam lithography process. Moreover, in the fabrication of single-layer graphene nanoribbons, it is found that the fabricated nanoribbons using nanowire etching masks showed a lower low-frequency noise level than those fabricated using polymer as etching masks.[22] In addition, the line-width roughness could be scaled down with the nanoribbon width.[23] Therefore, it is suggested that the above fabrication method may produce high-quality nanoribbons for transport studies.

For the device applications of nanowires and nanoribbons, it is desirable and important to obtain useful information about the carrier density and mobility, which is usually estimated from the characterization of FETs built on those 1-D nanomaterials. However, such calculation could have a large deviation because of the difficulty in accurately estimating the gate capacitance and the extrinsic effect of gate-induced electric field could also affect the estimated carrier mobility.[33,34] A more reliable method to quantify the intrinsic carrier density and mobility is

Received: January 29, 2016
Revised: March 28, 2016
Published: April 5, 2016

DOI: 10.1021/acs.nanolett.6b00398
Nano Lett. 2016, 16, 3109−3115

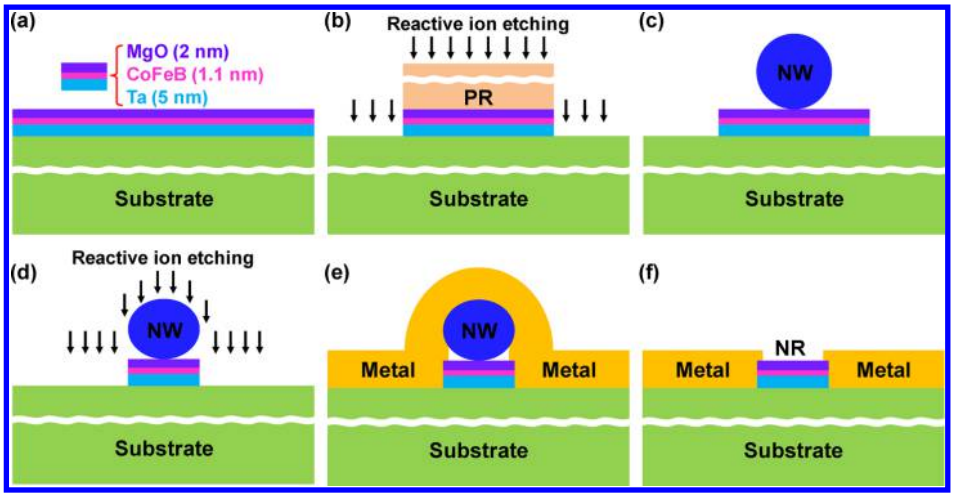

Figure 1. |Fabrication process flow of nanoribbons with self-aligned contacts using nanowires as both etching and deposition masks. (a) Start with the preparation of the channel material on a substrate, which in this study is a Ta/CoFeB/MgO stack sputtered on a Si/SiO_2 substrate. (b) Optical photolithography and subsequent reactive ion etching (RIE) to pattern the Ta/CoFeB/MgO film into micron-scale Hall bar geometry in order to reduce the film area. Large-size Cr/Au metal contact pads for future electrical probing and characterization are then defined by another optical photolithography and subsequent electron-beam evaporation. (c) Transfer SnO_2 nanowires (NWs) onto the substrate, with some SnO_2 nanowires lying on top of the Ta/CoFeB/MgO Hall bar. (d) Another RIE process to etch the Ta/CoFeB/MgO structure into nanoribbon (NR) using the SnO_2 nanowire as a mask. (e) Electron-beam lithography and subsequent metal deposition to define multiple contacts to the Ta/CoFeB/MgO nanoribbon. The metal deposition can be done by sputtering (conformal) or two steps of e-beam evaporation (directional): one tilted evaporation from the left side and the other one from the right side of the nanowire mask. (f) Ultrasonication to remove the nanowire mask, leaving the Ta/CoFeB/MgO nanoribbon with self-aligned metal contacts from the sidewall. The overlap of the metal electrode on the top surface of the nanoribbon depends on the metal deposition method.

using the Hall effect measurement, as widely adopted in bulk materials and thin films. Furthermore, anomalous Hall effect (AHE) measurement is a useful tool to characterize the magnetic property of ferromagnetic materials, in which the anomalous Hall resistivity is proportional to the magnetization.[35] However, the nanoscale geometry of nanowires and nanoribbons make it extremely challenging to define metal contacts for (anomalous) Hall effect measurements. Recently, this task has been achieved in hexagonal nanowires using electron beam lithography with high alignment accuracy, but the process was very challenging and required additional efforts for accurate alignment.[36,37] Alternatively, DeGrave et al. proposed an interesting method to make sidewall Hall contacts to nanoribbons using two-step electron-beam lithography and tilted metal deposition.[38] However, this method inherently led to undesired misalignment between the contact pairs for transverse voltage measurements, and hence, it required subsequent calculation to subtract the contribution from longitudinal voltage. Obtaining accurate results could become very difficult for AHE measurements in which both transverse and longitudinal signals are hysteretic.

In this work, we report a versatile method to fabricate nanoribbons with self-aligned metal contacts for (anomalous) Hall effect measurements using self-assembled nanowires as both etching and deposition masks. This convenient process only involves one-step electron beam lithography without the requirement of extremely high alignment accuracy. It is demonstrated that the metal contacts can be deposited using either sputtering or two-step electron beam evaporation. The width of the fabricated nanoribbon is scaled with the diameter of the nanowire mask, and it can be easily reduced down to tens of nanometers. For the proof-of-concept demonstration, we use this method to fabricate nanoribbons with a heavy metal/ferromagnet/oxide heterostructure to study the magnetization switching through current-induced spin−orbit torque (SOT) in the nanoscale regime, which exhibits distinct switching characteristics from micron-scale devices.

Nanoribbon Fabrication Process Flow. To start, material stacks consisting of $Ta/Co_{20}Fe_{60}B_{20}/MgO$ (5 nm/1.1 nm/2 nm in thickness) were deposited on a Si/SiO_2 substrate using magnetron sputtering (Figure 1a), followed by annealing at 200 °C for 30 min to enhance their perpendicular magnetic anisotropy (see more details of the film growth in Supporting Information S1).[39] After that, the Ta/CoFeB/MgO film was then patterned into a micron-scale Hall bar geometry (5 μm by 30 μm in dimension) using standard optical photolithography and reactive ion etching (RIE) as shown in Figure 1b, in order to reduce the film area and avoid electrical shorting in the following steps. Another optical photolithography step, followed by electron-beam evaporation, was carried out to define 10/100 nm Cr/Au contact pads for future electrical characterization. Then SnO_2 nanowires, synthesized by the conventional vapor−liquid−solid (VLS) method on a bare Si substrate,[40] were transferred on to the sample, and some nanowires lied on top of the Ta/CoFeB/MgO region to be used as etching masks, as shown in Figure 1c. The length of the SnO_2 nanowires was up to hundreds of micrometers with typical diameter ranging from 50 to 200 nm (see Supporting Information S2). Another RIE process was performed to transfer the 1-D morphology onto the underlying Ta/CoFeB/MgO structure using the SnO_2 nanowires as etching masks, as shown in Figure 1d. This process fabricated Ta/CoFeB/MgO heterostructure nanoribbons with widths no larger than the mask nanowire diameters. After that, electron-beam lithography using bilayer PMMA resists was used to define multiple contacts to the Ta/CoFeB/MgO nanoribbons. The subsequent metal deposition can be performed by either sputtering of Ti/Al (conformal deposition) or two-step tilted electron-beam evaporations of Cr/Au (directional deposition) from both sides of the nanowire mask, as shown in Figure 1e. Finally, the

DOI: 10.1021/acs.nanolett.6b00398
Nano Lett. 2016, 16, 3109−3115

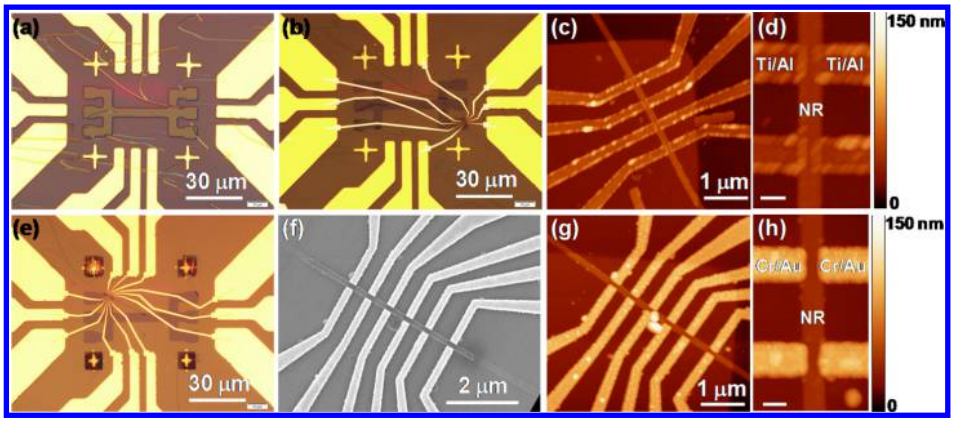

Figure 2. |Microscope images of the device fabrication. (a) Optical microscope image of a Ta/CoFeB/MgO micron-scale Hall bar structure after the transfer of SnO_2 nanowires. (b) Optical microscope image of the final device after etching, metal deposition, and ultrasonication. (c) AFM image of the fabricated Ta/CoFeB/MgO nanoribbon with self-aligned Ti/Al contacts using sputtering. (d) Enlarged AFM image of the 150 nm-wide Ta/CoFeB/MgO nanoribbon with self-aligned Ti/Al contacts. The distance between two transverse contact pairs is less than 30 nm. The scale bar equals to 150 nm. (e) Optical microscope image of another final device with Cr/Au contacts. (f) SEM image of the fabricated Ta/CoFeB/MgO nanoribbon with self-aligned Cr/Au contacts using two-step electron-beam evaporation. (g) Corresponding AFM image of the same device as in (f). (h) Enlarged AFM image of the 150 nm-wide Ta/CoFeB/MgO nanoribbon with self-aligned Cr/Au contacts. The distance between two transverse contact pairs is about 60 nm. The scale bar equals to 150 nm.

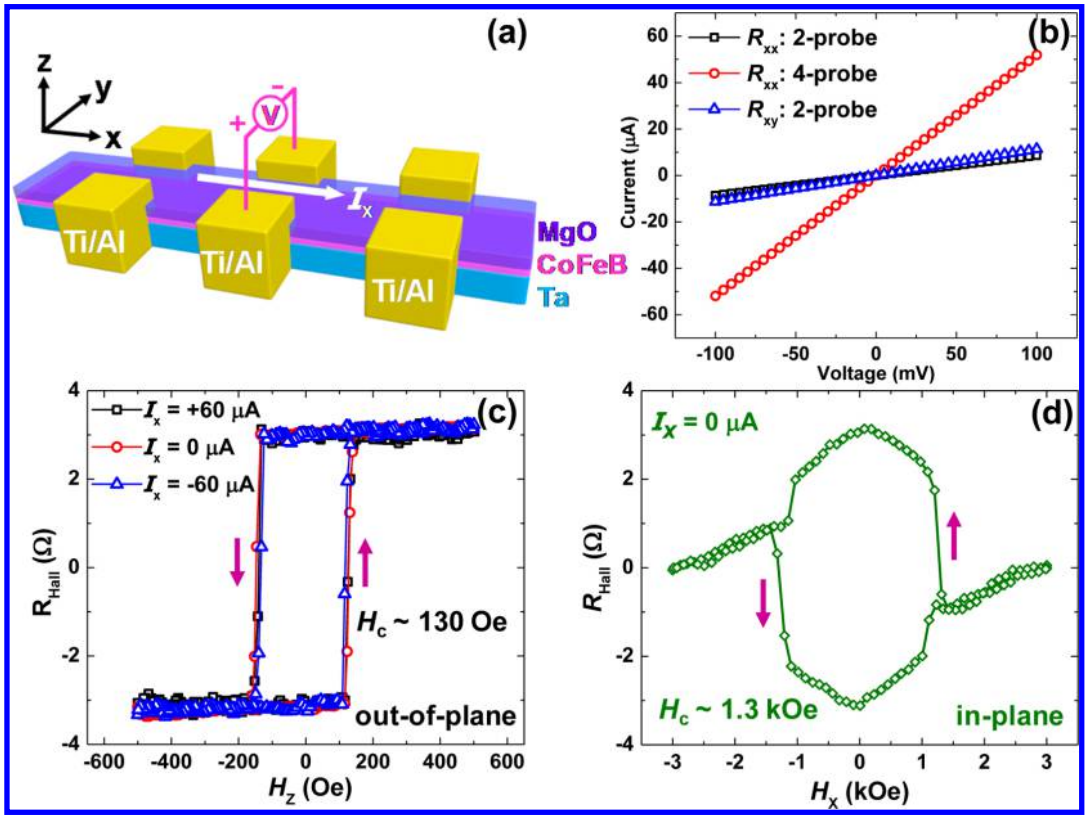

Figure 3. |Anomalous Hall measurements. (a) Schematic illustration of a Ta/CoFeB/MgO nanoribbon with self-aligned metal contacts. The setup for anomalous Hall effect measurement is also shown. (b) 2-Probe and 4-probe $I-V$ measurements between two adjacent contacts (R_{xx}) and two transverse contact pairs (R_{xy}). They all show linear $I-V$ characteristics, indicating reliable metal contacts to the nanoribbon. (c) Dependence of the anomalous Hall resistance R_{Hall} on the out-of-plane magnetic field H_z under various current biases, showing no apparent current-dependence. (d) Dependence of the anomalous Hall resistance R_{Hall} on the in-plane magnetic field H_x under zero dc current bias, showing a much bigger coercivity than the out-of-plane one.

sample was ultrasonicated in acetone to lift-off the metal layer with PMMA and also to remove the nanowire mask, leaving only the Ta/CoFeB/MgO nanoribbon with self-aligned metal contacts from the nanoribbon sidewall, as shown in Figure 1f. The overlap of the metal electrode on the nanoribbon top surface depends on the metal deposition method. In practice, this process can be easily translated to other thin films on arbitrary substrates, by carefully choosing the nanowire mask and the dry etching recipe. The width of the fabricated nanoribbon depends on the mask nanowire diameter, the

DOI: 10.1021/acs.nanolett.6b00398
Nano Lett. 2016, 16, 3109−3115

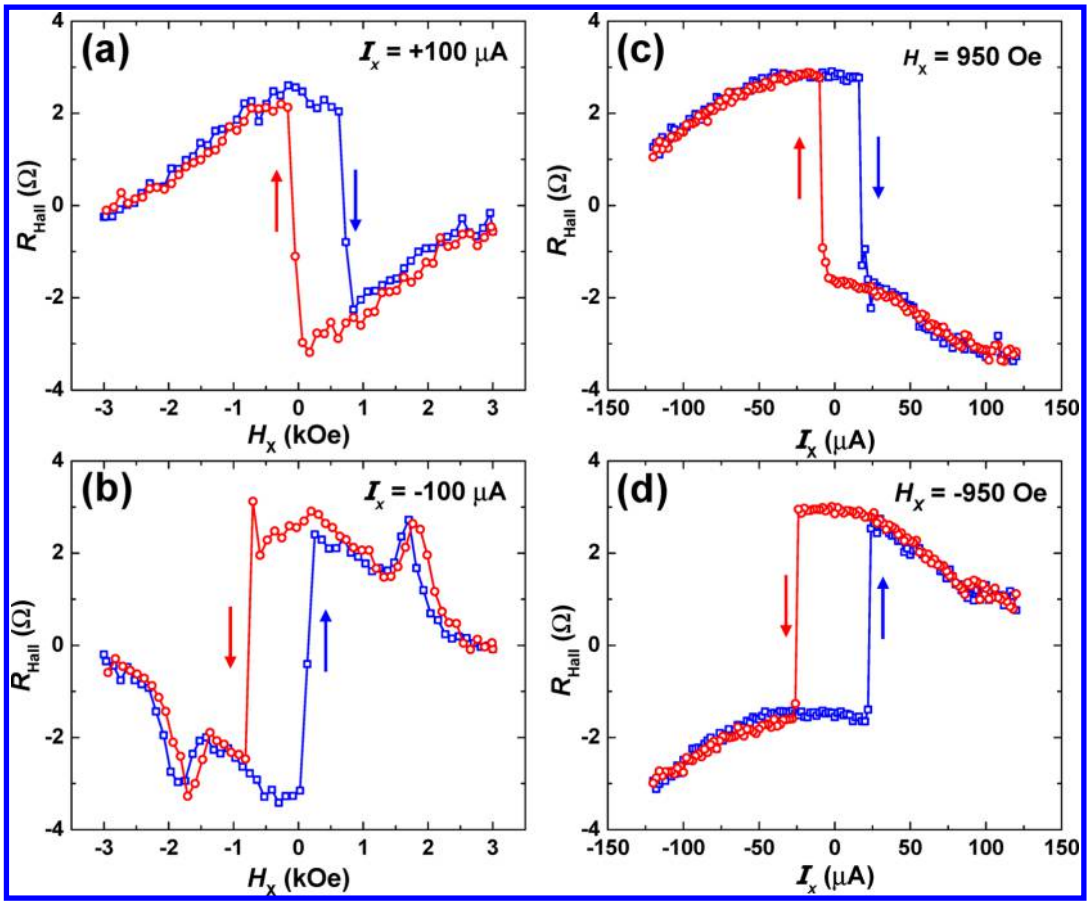

Figure 4. |Current-induced magnetization switching. (a,b) Dependence of the anomalous Hall resistance R_{Hall} on the in-plane magnetic field H_x at room temperature under different dc biases of I_x = 100 μA and I_x = −100 μA, respectively. (c,d) Current-induced magnetization switching at room temperature in the presence of constant in-plane magnetic fields of H_x = 950 Oe and H_x = −950 Oe, respectively.

original film thickness and also the etching recipe. Using this technique, the nanoribbon width can be possibly scaled down to sub-10 nm.

Device Structure and Characterizations. To demonstrate this method in practical device fabrication, Figure 2a shows the microscope image after transferring the VLS-synthesized SnO_2 nanowires on to the patterned Ta/CoFeB/MgO micron-scale Hall bar structure. Figure 2b shows the microscope image of the final device after etching it into nanoribbon and sputtering self-aligned Ti/Al (5 nm/25 nm in thickness) contacts. The final structure and surface morphology was inspected by an atomic force microscope (AFM), as shown in Figure 2c. From the zoom-in AFM image shown in Figure 2d, we can clearly see the fabricated Ta/CoFeB/MgO nanoribbon with sputtered self-aligned Ti/Al contacts in which the nanoribbon width was about 150 nm, and the distance between two transverse contact pairs was less than 30 nm. The fabricated nanoribbon width can be easily reduced down to about 40 nm when using nanowires with smaller diameters as etching masks (see Supporting Information S3 and S4). In this process, the two contact pairs were defined by one-step electron-beam lithography (line patterning perpendicular to the nanoribbon), so that the misalignment was minimized. Alternatively, two-step electron-beam evaporations of Cr/Au (10 nm/50 nm in total thickness) can be used to define another type of metal contacts, and the microscope image of the final device is shown in Figure 2e. The scanning electron microscope (SEM) image in Figure 2f clearly shows a Ta/CoFeB/MgO nanoribbon with six Cr/Au contacts on each side, and Figure 2g shows the corresponding AFM image of the same device. Again, from the zoom-in AFM image shown in Figure 2h, we can clearly see the fabricated Ta/CoFeB/MgO nanoribbon with two self-aligned Cr/Au contacts on each side in which the nanoribbon width was about 150 nm, and the distance between two transverse contact pairs was about 60 nm. Compared with the previous case using sputtering deposition (shown in Figure 2d), the metal contact deposited using electron-beam evaporation had a smoother edge and less overlap on the nanoribbon top surface (Figure 2h). Nonetheless, both approaches have been demonstrated to be capable to make reliable contacts to the fabricated nanoribbon.

Figure 3a shows the schematic illustration of the fabricated Ta/CoFeB/MgO nanoribbon with self-aligned metal contacts. $I-V$ measurements between two adjacent contacts (R_{xx}) using both 2-probe and 4-probe techniques were performed at room temperature to test the contact quality, showing linear characteristics in Figure 3b. The contact resistance ($R_{cont} \approx 4$ kΩ) was estimated to be on the same order of the metallic channel resistance ($R_{ch} \approx 2$ kΩ) in this device. Meanwhile, the 2-probe $I-V$ measurement between two transverse contact pairs (R_{xy}) showed a comparable resistance with that between two adjacent contacts (R_{xx}), indicating that these self-aligned contacts were functioning. Using these self-aligned contacts and the setup illustrated in Figure 3a, AHE measurements were performed on the Ta/CoFeB/MgO nanoribbon under both out-of-plane and in-plane magnetic fields, and the results are

DOI: 10.1021/acs.nanolett.6b00398
Nano Lett. 2016, 16, 3109−3115

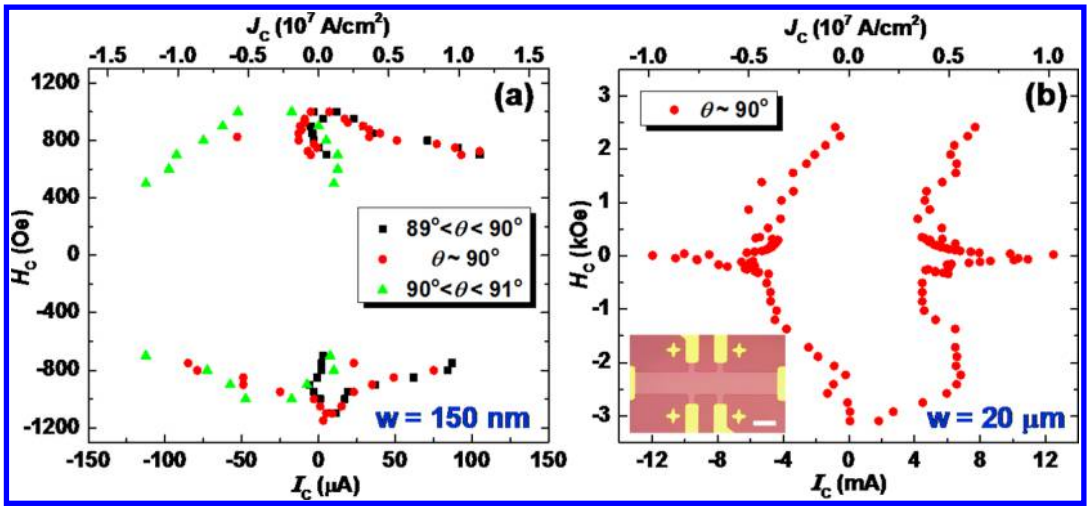

Figure 5. |Comparison of switching phase diagrams. (a) Switching phase diagram of the Ta/CoFeB/MgO nanoribbon (w = 150 nm) with slightly different magnetic field directions. (b) Switching phase diagram of a micron-scale Ta/CoFeB/MgO Hall bar structure (dimension of 20 μm by 40 μm) with nominal in-plane magnetic field direction. The inset shows the device microscope image and the scale bar equals to 20 μm. The corresponding current densities in both (a) and (b) are shown in the top axes.

shown in Figures 3c,d, respectively. The magneto-transport measurements were performed using a standard lock-in technique in a Quantum Design Physical Parameter Measurement System (PPMS) with horizontal rotator option. The ac current I_{ac} = 1 μA at f = 1 kHz, dc bias was applied by a Keithley 6221 dc/ac current source, and the voltage was sensed by a SR830 lock-in amplifier. In Figure 3c, the out-of-plane switching behavior did not show an apparent dependence on the charge current density, while the effect on the in-plane switching behavior will be discussed in details later in Figure 4. The out-of-plane coercivity was about $H_c \approx$ 130 Oe, much smaller than the in-plane coercivity of $H_c \approx$ 1300 Oe, which affirmed that the perpendicular magnetic anisotropy in the original Ta/CoFeB/MgO film was nicely preserved during the nanoribbon fabrication process. It also suggested that the potential damage on the nanometer-thick Ta/CoFeB/MgO magnetic stacks during the dry etching and gentle sonication processes was rather minor. This is also supported by detailed analysis on the surface roughness and also line-width roughness of the resulting Ta/CoFeB/MgO nanoribbon (see Supporting Information S5).

Current-Induced Magnetization Switching in Nanoscale Regime. The study of electrical manipulation of magnetization is of both physical interest and technological importance,[39,41−44] and it shows appealing applications in nonvolatile memory and low-power logic devices.[45] In the past few years, tremendous progress has been made in the current-induced SOT-driven magnetization switching in a heavy metal/ferromagnet heterostructure with perpendicular magnetic anisotropy through spin torque from the spin Hall effect.[14,39,41−43] So far, most studies of SOT-driven magnetization switching have been carried out in micron-scale Hall-bar devices. It is of great interest to investigate the switching behavior and dynamics in the nanoscale regime. For example, it is suggested that for narrow wires, the shape anisotropy could facilitate the SOT-induced domain wall motion in the absence of external magnetic field.[46] However, as the device dimension scales down, it becomes more and more challenging to fabricate nanoscale Hall bar structure for AHE measurements. Our versatile method developed in this work can be readily used to make nanoscale Hall bar with self-aligned metal contacts deposited without the need for extremely high alignment accuracy. Typical AHE data in Figure 3 were obtained from a Ta/CoFeB/MgO nanoribbon Hall bar structure to illustrate the success of this approach.

Using the fabricated heavy metal/ferromagnet nanostructure, we have performed the in-plane AHE measurement on the Ta/CoFeB/MgO nanoribbon under different dc biases of I_x = 100 μA (equivalent to a current density of J_x = 1.1 × 10^7 A/cm^2) and I_x = −100 μA, as shown in Figure 4a,b, respectively. Compared with the in-plane AHE data under zero dc bias shown previously in Figure 3d, it is found that the in-plane coercivity was dramatically reduced to $H_c \approx$ 400 Oe in the presence of a large dc bias. Also, the switching curves were not centered at zero magnetic field, which could be attributed to the possibility that the applied magnetic field did not perfectly align along the nanoribbon axis. Alternatively, we can realize charge current-induced magnetization switching by sweeping the dc bias in the presence of a constant external in-plane magnetic field along the charge current direction. Figures 4c,d show the cases with in-plane magnetic fields of H_x = 950 Oe and H_x = −950 Oe, respectively. It can be seen that opposite bias currents or in-plane magnetic fields led to opposite hysteretic switching behaviors because the directions of the current-induced SOTs are opposite, which favored opposite magnetization states.[42] This characteristic is consistent with the current-induced SOT switching in micron-scale heavy metal/ferromagnet heterostructure (see Supporting Information S6 for comparison).[39] In general, the favored magnetization state is determined by the effective field induced by the spin-Hall-effect-SOT, which is given by[47]

$$\vec{H}_{SHE} = -\tau_1^{SHE}(\hat{m} \times (\hat{z} \times \hat{j})) \quad (1)$$

where $\hat{m}$, $\hat{z}$, and $\hat{j}$ are the unit vectors along the magnetization direction, the z-axis, and the charge current flow, respectively. In general, the magnitude of the SOT is defined as $\tau_1^{SHE} = \frac{\hbar\theta_{SHE}J}{2|e|M_s t_F}$, where $\hbar$ is the reduced Planck constant, θ_{SHE} is the spin Hall angle, J is the charge current density, e is the electron charge, M_s is the saturation magnetization, and t_F is the thickness of the ferromagnetic layer. In the geometry of our experiments, the charge current flows along the x-axis ($\hat{j}//\hat{x}$),

DOI: 10.1021/acs.nanolett.6b00398
Nano Lett. 2016, 16, 3109−3115

and $\hat{m}$ is tilted away from the z-axis in the $x-z$ plane. It is clear from eq 1 that whenever the charge current direction (I_x or equivalently $\hat{j}$) or the magnetic field direction (H_x or equivalently $\hat{m}$) is changed, the effective field direction is reversed, and hence the favored magnetization direction is also reversed.

Furthermore, we have performed extensive current-induced magnetization switching measurements under various in-plane magnetic fields, so that a switching phase diagram can be constructed, as shown in Figure 5a. In the case with nominal in-plane magnetic field ($\theta = 90°$), the switching phase diagram is more or less symmetric for negative magnetic fields (bottom half, $H_c < 0$); however, it becomes highly asymmetric for positive magnetic fields (top half, $H_c > 0$), shifting toward the positive current regime ($I_c > 0$). Such asymmetry can be also seen clearly from Figure 4c,d, and again it could be attributed to the imperfect alignment between the in-plane magnetic field and the nanoribbon axis. Moreover, as we slightly change the angle between the in-plane magnetic field and the nanoribbon axis by less than $\pm 1°$, such asymmetry becomes more prominent, as shown in Figure 5a. In the slightly tilted case of $89° < \theta < 90°$, the switching phase diagram become symmetric with respect to the switching field, but it shifts to the positive current regime ($I_c > 0$). This result suggests that the magnetization is more easily switched for negative current than positive one, as the system favors one magnetization state defined by the out-of-plane component of the misaligned magnetic field. Similarly, as the magnetic field is tilted toward the other direction, that is, $90° < \theta < 91°$, the switching current asymmetry shifts to the other side ($I_c < 0$) because the system favors the opposite magnetization state defined by the out-of-plane component of the misaligned magnetic field. For comparison, we have fabricated micron-scale Hall bar devices (20 μm by 40 μm in dimension) on the same Ta/CoFeB/MgO film using optical photolithography and then performed the same current-induced magnetization switching measurements to obtain the switching phase diagram as shown in Figure 5b. We can see that it does not resemble the same switching behavior in the nanoscale Hall bar device. The discrepancy suggests that the size effect could have a significant effect on the switching dynamics in the heavy metal/ferromagnet heterostructure. A systematic study on the size-dependent switching is required in the future to understand the underlying mechanism. Again, the versatile method developed in this work could provide a useful platform to fabricate such devices with different dimensions down to tens of nanometers. It could also open up new possibilities to study the magnetic domain wall dynamics as well as charge and spin transport in the nanoscale regime in order to further build novel spintronic devices.

In summary, we have developed a versatile fabrication method to make nanoribbons with self-aligned contacts using self-assembled nanowires as both etching and deposition masks. The fabricated structures could be readily used for (anomalous) Hall effect measurements in the nanoscale regime. By tuning the mask nanowire diameter and etching recipe, the fabricated nanoribbon width was easily scaled down to tens of nanometers. It is shown that the metal contacts can be deposited using either conformal sputtering method or directional electron-beam evaporation, and it did not require extremely high alignment accuracy. As a proof-of-concept demonstration, we used this method to fabricate nanoribbons from Ta/CoFeB/MgO thin film sputtered on a Si/SiO_2 substrate using VLS-synthesized SnO_2 nanowires as masks. Extensive magneto-transport measurements have been performed to further study the current-induced magnetization switching through spin torque from the spin Hall effect in the nanoscale regime. The switching behavior is found to be very different from that in micron-scale devices, implying the size effect in the magnetic dynamics. In general, this convenient fabrication process can be readily transferred to other materials on arbitrary substrates; therefore, it provides a useful tool to explore the charge and spin transport in solid-state materials in the nanoscale regime.

■ ASSOCIATED CONTENT

Supporting Information

The Supporting Information is available free of charge on the ACS Publications website at DOI: 10.1021/acs.nanolett.6b00398.

Preparation of the Ta/$Co_{20}Fe_{60}B_{20}$/MgO film. SEM images of VLS-synthesized SnO_2 nanowires. Fabrication of Ta/CoFeB/MgO nanoscale Hall device with smaller dimensions. SEM images of a Ta/CoFeB/MgO nanoribbon cross. Roughness analysis on the fabricated nanoribbon. Current-induced magnetization switching in micron-scale Ta/CoFeB/MgO device (PDF)

■ AUTHOR INFORMATION

Corresponding Authors

*E-mail: tjianshi@ucla.edu.
*E-mail: wang@seas.ucla.edu.

Present Addresses

(J.T.) IBM Thomas J. Watson Research Center, Yorktown Heights, New York 10598, United States.
(W.J.) Materials Science Division, Argonne National Laboratory, Argonne, Illinois 60439, United States.

Notes

The authors declare no competing financial interest.

■ ACKNOWLEDGMENTS

The authors acknowledge the funding supports from National Science Foundation through grant ECCS 1308358 and from National Science Council through grant No. MOST 103-2218-E-011-007-MY3. This work was partially supported by the Defense Advanced Research Projects Agency (DARPA) programme on Nonvolatile Logic (NVL) and in part by the National Science Foundation Nanosystems Engineering Research Center for Translational Applications of Nanoscale Multiferroic Systems (TANMS). This work was also supported in part by the Function Accelerated nanoMaterial Engineering Center, one of six centres of Semiconductor Technology Advanced Research network, a Semiconductor Research Corporation programme sponsored by Microelectronics Advanced Research Corporation and DARPA. K.W. acknowledges the support of the Raytheon endowed chair professorship.

■ REFERENCES

(1) Lu, W.; Xie, P.; Lieber, C. M. *IEEE Trans. Electron Devices* **2008**, *55* (11), 2859−2876.
(2) Huang, Y.; Duan, X.; Cui, Y.; Lauhon, L. J.; Kim, K. H.; Lieber, C. M. *Science* **2001**, *294* (5545), 1313−1317.
(3) Colinge, J.-P.; Lee, C.-W.; Afzalian, A.; Akhavan, N. D.; Yan, R.; Ferain, I.; Razavi, P.; O'Neill, B.; Blake, A.; White, M.; Kelleher, A.-M.; McCarthy, B.; Murphy, R. *Nat. Nanotechnol.* **2010**, *5* (3), 225−229.

DOI: 10.1021/acs.nanolett.6b00398
Nano Lett. 2016, 16, 3109−3115

(4) Tang, J.; Wang, C.-Y.; Xiu, F.; Lang, M.; Chu, L.-W.; Tsai, C.-J.; Chueh, Y.-L.; Chen, L.-J.; Wang, K. L. *ACS Nano* **2011**, *5* (7), 6008−6015.
(5) Bai, J.; Duan, X.; Huang, Y. *Nano Lett.* **2009**, *9* (5), 2083−2087.
(6) Wang, Z. L. *Mater. Sci. Eng., R* **2009**, *64*, 33−71.
(7) Cui, Y.; Wei, Q.; Park, H.; Lieber, C. M. *Science* **2001**, *293* (5533), 1289−1292.
(8) Sun, Y.; Choi, W. M.; Jiang, H.; Huang, Y. Y.; Rogers, J. a. *Nat. Nanotechnol.* **2006**, *1* (3), 201−207.
(9) Elfström, N.; Karlström, A. E.; Linnros, J. *Nano Lett.* **2008**, *8* (3), 945−949.
(10) Huang, M. H.; Mao, S.; Feick, H.; Yan, H.; Wu, Y.; Kind, H.; Weber, E.; Russo, R.; Yang, P. *Science* **2001**, *292* (5523), 1897−1899.
(11) Duan, X.; Huang, Y.; Agarwal, R.; Lieber, C. M. *Nature* **2003**, *421* (6920), 241−245.
(12) Law, M.; Greene, L. E.; Johnson, J. C.; Saykally, R.; Yang, P. *Nat. Mater.* **2005**, *4* (6), 455−459.
(13) Tang, J.; Wang, C.-Y.; Chang, L.-T.; Fan, Y.; Nie, T.; Chan, M.; Jiang, W.; Chen, Y.-T.; Yang, H.-J.; Tuan, H.-Y.; Chen, L.-J.; Wang, K. L. *Nano Lett.* **2013**, *13* (9), 4036−4043.
(14) Emori, S.; Bauer, U.; Ahn, S.-M.; Martinez, E.; Beach, G. S. D. *Nat. Mater.* **2013**, *12* (7), 611−616.
(15) Carignan, L.-P.; Yelon, A.; Menard, D.; Caloz, C. *IEEE Trans. Microwave Theory Tech.* **2011**, *59* (10), 2568−2586.
(16) Son, Y.-W.; Cohen, M. L.; Louie, S. G. *Nature* **2006**, *444* (7117), 347−349.
(17) Wang, N.; Cai, Y.; Zhang, R. Q. *Mater. Sci. Eng., R* **2008**, *60* (1−6), 1−51.
(18) Chen, S.; Bomer, J. G.; van der Wiel, W. G.; Carlen, E. T.; van den Berg, A. *ACS Nano* **2009**, *3* (11), 3485−3492.
(19) Jiao, L.; Wang, X.; Diankov, G.; Wang, H.; Dai, H. *Nat. Nanotechnol.* **2010**, *5* (5), 321−325.
(20) Ko, H. C.; Baca, A. J.; Rogers, J. A. *Nano Lett.* **2006**, *6* (10), 2318−2324.
(21) Baringhaus, J.; Ruan, M.; Edler, F.; Tejeda, A.; Sicot, M.; Taleb-Ibrahimi, A.; Li, A.-P.; Jiang, Z.; Conrad, E. H.; Berger, C.; Tegenkamp, C.; de Heer, W. a. *Nature* **2014**, *506* (7488), 349−354.
(22) Xu, G.; Bai, J.; Torres, C. M.; Song, E. B.; Tang, J.; Zhou, Y.; Duan, X.; Zhang, Y.; Wang, K. L. *Appl. Phys. Lett.* **2010**, *97* (7), 073107.
(23) Xu, G.; Torres, C. M.; Bai, J.; Tang, J.; Yu, T.; Huang, Y.; Duan, X.; Zhang, Y.; Wang, K. L. *Appl. Phys. Lett.* **2011**, *98* (24), 243118.
(24) Fasoli, A.; Colli, A.; Lombardo, A.; Ferrari, A. C. *Phys. Status Solidi B* **2009**, *246* (11−12), 2514−2517.
(25) Liao, L.; Bai, J.; Cheng, R.; Lin, Y.-C.; Jiang, S.; Huang, Y.; Duan, X. *Nano Lett.* **2010**, *10* (5), 1917−1921.
(26) Liao, L.; Bai, J.; Lin, Y.-C.; Qu, Y.; Huang, Y.; Duan, X. *Adv. Mater.* **2010**, *22* (17), 1941−1945.
(27) Kang, C. G.; Kang, J. W.; Lee, S. K.; Lee, S. Y.; Cho, C. H.; Hwang, H. J.; Lee, Y. G.; Heo, J.; Chung, H.-J.; Yang, H.; Seo, S.; Park, S.-J.; Ko, K. Y.; Ahn, J.; Lee, B. H. *Nanotechnology* **2011**, *22* (29), 295201.
(28) Xu, W.; Seo, H.-K.; Min, S.-Y.; Cho, H.; Lim, T.-S.; Oh, C.; Lee, Y.; Lee, T.-W. *Adv. Mater.* **2014**, *26* (21), 3459−3464.
(29) Kang, S. H.; Hwang, W. S.; Lin, Z.; Kwon, S. H.; Hong, S. W. *Nano Lett.* **2015**, *15* (12), 7913−7920.
(30) Liao, L.; Lin, Y.-C.; Bao, M.; Cheng, R.; Bai, J.; Liu, Y.; Qu, Y.; Wang, K. L.; Huang, Y.; Duan, X. *Nature* **2010**, *467* (7313), 305−308.
(31) Liao, L.; Bai, J.; Cheng, R.; Lin, Y.-C.; Jiang, S.; Qu, Y.; Huang, Y.; Duan, X. *Nano Lett.* **2010**, *10* (10), 3952−3956.
(32) Liao, L.; Bai, J.; Cheng, R.; Zhou, H.; Liu, L.; Liu, Y.; Huang, Y.; Duan, X. *Nano Lett.* **2012**, *12* (6), 2653−2657.
(33) Wunnicke, O. *Appl. Phys. Lett.* **2006**, *89* (8), 083102.
(34) Tang, J.; Wang, C. Y.; Hung, M. H.; Jiang, X.; Chang, L.-T.; He, L.; Liu, P. H.; Yang, H. J.; Tuan, H. Y.; Chen, L. J.; Wang, K. L. *ACS Nano* **2012**, *6* (6), 5710−5717.
(35) Jiang, W.; Zhou, X. Z.; Williams, G. *Phys. Rev. B: Condens. Matter Mater. Phys.* **2010**, *82* (14), 144424.
(36) Storm, K.; Halvardsson, F.; Heurlin, M.; Lindgren, D.; Gustafsson, A.; Wu, P. M.; Monemar, B.; Samuelson, L. *Nat. Nanotechnol.* **2012**, *7* (11), 718−722.
(37) Blömers, C.; Grap, T.; Lepsa, M. I.; Moers, J.; Trellenkamp, S.; Grützmacher, D.; Lüth, H.; SchäPers, T. *Appl. Phys. Lett.* **2012**, *101* (15), 152106.
(38) DeGrave, J. P.; Liang, D.; Jin, S. *Nano Lett.* **2013**, *13* (6), 2704−2709.
(39) Yu, G.; Upadhyaya, P.; Wong, K. L.; Jiang, W.; Alzate, J. G.; Tang, J.; Amiri, P. K.; Wang, K. L. *Phys. Rev. B: Condens. Matter Mater. Phys.* **2014**, *89* (10), 104421.
(40) He, J. H.; Wu, T. H.; Hsin, C. L.; Li, K. M.; Chen, L. J.; Chueh, Y. L.; Chou, L. J.; Wang, Z. L. *Small* **2006**, *2* (1), 116−120.
(41) Liu, L.; Pai, C.-F.; Li, Y.; Tseng, H. W.; Ralph, D. C.; Buhrman, R. A. *Science* **2012**, *336* (6081), 555−558.
(42) Liu, L.; Lee, O. J.; Gudmundsen, T. J.; Ralph, D. C.; Buhrman, R. A. *Phys. Rev. Lett.* **2012**, *109* (9), 096602.
(43) Yu, G.; Upadhyaya, P.; Fan, Y.; Alzate, J. G.; Jiang, W.; Wong, K. L.; Takei, S.; Bender, S. a; Chang, L.-T.; Jiang, Y.; Lang, M.; Tang, J.; Wang, Y.; Tserkovnyak, Y.; Amiri, P. K.; Wang, K. L. *Nat. Nanotechnol.* **2014**, *9* (7), 548−554.
(44) Miron, I. M.; Garello, K.; Gaudin, G.; Zermatten, P.-J.; Costache, M. V.; Auffret, S.; Bandiera, S.; Rodmacq, B.; Schuhl, A.; Gambardella, P. *Nature* **2011**, *476* (7359), 189−193.
(45) Wang, K. L.; Alzate, J. G.; Khalili Amiri, P. *J. Phys. D: Appl. Phys.* **2013**, *46* (7), 074003.
(46) Haazen, P. P. J.; Murè, E.; Franken, J. H.; Lavrijsen, R.; Swagten, H. J. M.; Koopmans, B. *Nat. Mater.* **2013**, *12* (4), 299−303.
(47) Khvalkovskiy, a. V.; Cros, V.; Apalkov, D.; Nikitin, V.; Krounbi, M.; Zvezdin, K. a.; Anane, A.; Grollier, J.; Fert, A. *Phys. Rev. B: Condens. Matter Mater. Phys.* **2013**, *87* (2), 020402.

DOI: 10.1021/acs.nanolett.6b00398
Nano Lett. 2016, 16, 3109−3115